Key Points:
- An evolutionary algorithm has been applied to the estimation of cloud glaciation temperature (CGT)
- CGT varies with height, exhibiting a minimum in the upper and a maximum in the midtroposphere
- The vertical, latitudinal, and land-sea variation of the cloud top CGT need to be further explored

Correspondence to:
C. Hoose,
corinna.hoose@kit.edu

Cloud glaciation temperature estimation from passive remote sensing data with evolutionary computing

L. Carro-Calvo[1,2], C. Hoose[1], M. Stengel[3], and S. Salcedo-Sanz[4]

[1]Institute of Meteorology and Climate Research, Karlsruhe Institute of Technology, Karlsruhe, Germany, [2]Now at Department of Astrophysics and Atmospheric Sciences, Universidad Complutense de Madrid, Madrid, Spain, [3]Deutscher Wetterdienst, Offenbach, Germany, [4]Department of Signal Processing and Communications, Universidad de Alcalá, Madrid, Spain

Abstract The phase partitioning between supercooled liquid water and ice in clouds in the temperature range between 0 and −37°C influences their optical properties and the efficiency of precipitation formation. Passive remote sensing observations provide long-term records of the cloud top phase at a high spatial resolution. Based on the assumption of a cumulative Gaussian distribution of the ice cloud fraction as a function of temperature, we quantify the cloud glaciation temperature (CGT) as the 50th percentile of the fitted distribution function and its variance for different cloud top pressure intervals, obtained by applying an evolutionary algorithm (EA). EAs are metaheuristics approaches for optimization, used in difficult problems where standard approaches are either not applicable or show poor performance. In this case, the proposed EA is applied to 4 years of Pathfinder Atmospheres-Extended (PATMOS-x) data, aggregated into boxes of 1°×1° and vertical layers of 5.5 hPa. The resulting vertical profile of CGT shows a characteristic sickle shape, indicating low CGTs close to homogeneous freezing in the upper troposphere and significantly higher values in the midtroposphere. In winter, a pronounced land-sea contrast is found at midlatitudes, with lower CGTs over land. Among this and previous studies, there is disagreement on the sign of the land-sea difference in CGT, suggesting that it is strongly sensitive to the detected and analyzed cloud types, the time of the day, and the phase retrieval method.

1. Introduction

The phase transition from liquid water to ice in mixed-phase clouds (in the temperature range between 0 and approximately −37°C) influences precipitation type and intensity, cloud lifetime, cloud electrical charges, cloud optical properties, and other variables which are important for the Earth's water and energy budgets [*Pruppacher and Klett*, 1997]. In different cloud types and environments, the glaciation (the change from a predominantly liquid state to a predominantly ice state) occurs at different glaciation temperatures [e.g., *Williams et al.*, 2002], which are difficult to represent in weather or climate models and therefore cause large uncertainties in the forecasted precipitation and the cloud radiative forcing [*Waliser et al.*, 2009], in particular, in regions where the phase distribution deviates significantly from the global average, e.g., the Southern Oceans [*Forbes and Ahlgrimm*, 2014; *McCoy et al.*, 2015; *Kay et al.*, 2016].

On a microphysical scale, the phase transition of individual droplets can occur either via homogeneous freezing at temperatures of approximately −37°C or with the help of an aerosol as ice nucleating particle at higher temperatures [*Hoose and Möhler*, 2012]. Once the first crystals have formed, they can grow on the expense of evaporating droplets (Wegener-Bergeron-Findeisen process) [*Findeisen*, 1938] and/or induce ice multiplication processes [*Hallett and Mossop*, 1974], both of which may rapidly lead to a full glaciation of the cloud. Therefore, observed ice mass fractions (cloud ice divided by total cloud water) are typically either close to 0 or close to 1, with a low frequency of occurrence of intermediate values [*Korolev et al.*, 2003; *Lloyd et al.*, 2015]. However, the concentration of ice nucleating particles and their ice nucleation activity depends on the properties of the ambient aerosol population and thus on location, altitude, and season. Additionally, the Wegener-Bergeron-Findeisen process only occurs in a limited range of conditions. If the updraft is strong enough, supercooled liquid water can be sustained and even grow in the presence of ice [*Korolev*, 2007]. As a

result, the temperature that a cloud top has to reach to change its state from predominantly (more than 50%) liquid water to predominantly ice (called the *cloud glaciation temperature* (CGT)) can assume values between approximately −5° and −37°C. In most cases, the CGT is not directly observable, because the microphysical evolution of individual clouds is difficult to track. Instead, statistical information on the occurrence of ice and liquid clouds as a function of temperature can be used to define the CGT as the 50th percentile of the cumulative distribution of the supercooled liquid or ice cloud fraction (the cloud phase distribution).

Measurements of the cloud phase distribution can be taken either by in situ instruments on aircrafts or mountain top stations or by active or passive ground- or space-based remote sensing. In situ sampling by aircraft can only cover a limited region, a relatively small number of events and is restricted to relatively shallow clouds due to the icing hazard. In a collection of data from predominantly stratiform clouds over Canada [*Korolev et al.*, 2003], more than 50% of all cloud segments consisted mostly of ice at temperatures below −10°C. In a different data set, frontal clouds over the British Isles showed even higher glaciation temperatures [*Bower et al.*, 1996]. In contrast, *Rosenfeld and Woodley* [2000] identified liquid droplets in a flight through a deep convective cloud down to temperatures of −37.5°C, probably due to the high vertical velocity and resulting high supersaturation. Ground-based remote sensing by cloud radar or lidar is also confined to a relatively small number of appropriately equipped sites [*Hogan et al.*, 2003; *Wolters et al.*, 2008; *Naud et al.*, 2010; *Bühl et al.*, 2016] and cannot detect the cloud phase at the relevant levels if liquid cloud or precipitation layers below obscure the view.

Active remote sensing from space, notably the Cloud and Aerosol Lidar with Orthogonal Polarization (CALIOP) instrument on board the Cloud-Aerosol Lidar and Infrared Pathfinder Satellite Observations (CALIPSO) mission [*Winker et al.*, 2010], offers relatively accurate phase retrievals because liquid and ice can be distinguished by the depolarization signal. CALIOP can yield vertical profiles of the phase distribution within the cloud, up to saturation of the signal (at an optical thickness higher than approximately 5) [*Winker et al.*, 2010]. However, the derived cloud phase distribution depends on details of the data analysis and/or the analysed time span: *Choi et al.* [2010b] derive the global average temperature with a supercooled liquid cloud fraction of 50% to be approximately −20°C, based on 12 months of CALIOP data (version 2.01, 2006–2007) and cloud temperatures from reanalyses. *Hu et al.* [2010] report a significantly colder temperature (−25°C) for a global mean supercooled liquid cloud fraction of 50%, when using CALIOP version 2.01 nighttime data from 2008 and the CALIPSO infrared imaging radiometer for the cloud temperature. Finally, *Komurcu et al.* [2014] derived approximately −15°C as the temperature with a global average supercooled liquid cloud fraction of 50% based on a longer time series (2008–2011) of CALIOP version 3 data and reanalysis cloud temperatures. A limitation of the CALIOP data set is the small spatial coverage due to the narrow instrument swath.

Passive remote sensing instruments on satellites can provide a much better temporal and spatial coverage of the Earth and thus offer the possibility to derive climatologies. However, the cloud phase can only be derived for the cloud top and not for the lower layers. As cloud tops are the coldest part of the clouds, freezing is expected to initiate here, making the cloud top a preferred region of interest. But it should be noted that in situations when ice particles formed at the cloud top sediment to lower layers and grow there, the cloud top phase distribution will be different from the in-cloud phase distribution. Retrieval algorithms for the cloud phase are available for polar orbiting instruments (e.g., the Moderate Resolution Imaging Spectroradiometer (MODIS) [*Platnick et al.*, 2003; *Baum et al.*, 2012], the Advanced Very High Resolution Radiometer (AVHRR) [*Pavolonis et al.*, 2005], and the Atmospheric Infrared Sounder (AIRS) [*Jin and Nasiri*, 2014; *Kahn et al.*, 2014] and for geostationary instruments such as the Spinning Enhanced Visible and Infrared Imager (SEVIRI) [*Wolters et al.*, 2008; *Stengel et al.*, 2014]. *Choi et al.* [2010a] show good agreement between the MODIS liquid cloud fraction and the CALIOP liquid cloud top fraction for Antarctic clouds. According to *Jin and Nasiri* [2014], AIRS liquid and ice phase pixels are misclassified about 1% of the time when compared with CALIOP, but a high percentage of AIRS pixels are reported as unknown phase. *Wolters et al.* [2008] compared different phase retrieval schemes for SEVIRI to a ground-based site in the Netherlands and concluded that all methods show high accuracy during summer but exhibit larger errors in winter. In *Yuan et al.* [2010] a technique for CGT estimation in convective clouds is presented based on MODIS data, using the nonmonotonous behavior of the cloud particle size with temperature.

The cloud phase information can be used for a direct analysis of the observed cloud systems, such as by *Naud et al.* [2006], who used MODIS cloud top phase information to characterize midlatitude winter storms, relating the cloud top phase to dynamical features within the cyclones. In *Rosenfeld et al.* [2011], the CGT of growing

convective cloud towers was estimated following the methodology of *Yuan et al.* [2010] and linked to the impact of different aerosol types.

In addition, observed cloud phase distributions and CGT have been used to evaluate and improve numerical weather prediction and global climate models [*Doutriaux-Boucher and Quaas*, 2004; *Forbes and Ahlgrimm*, 2014; *Komurcu et al.*, 2014; *Tan and Storelvmo*, 2016a]. It has been shown that the assumptions on the temperature dependence of the cloud phase in global climate models has significant implications for the simulated cloud feedbacks and climate sensitivity [*Mitchell et al.*, 1989; *Li and Le Treut*, 1992; *Choi et al.*, 2014; *Tan et al.*, 2016b].

In this paper we propose a novel CGT estimation technique from a multiyear data set of passive remote sensing satellite data, based on the assumption of a Gaussian distribution of the liquid and ice cloud top partitioning at different altitudes. The parameters of the Gaussian distribution for different cloud top pressure intervals are jointly estimated using an evolutionary algorithm (EA) [*Eiben and Smith*, 2003; *Goldberg*, 1989]. EAs have been previously applied to problems in meteorology and cloud physics [*Babb et al.*, 1999; *Bravy et al.*, 2002; *Cerdeña et al.*, 2006; *Pallavi and Vaithiyanathan*, 2013; *Ahn and Lee*, 2016], but to the best of our knowledge, they have not been yet considered in applications related to CGT analysis. In this case, classical approaches are not straightforward to be applicable to this nonlinear problem, whereas EAs are known to be very effective independently of the type of objective function, and they can cope with the integral formulation of the proposed model and the large number of parameters to be optimized. Note that the proposed EA methodology allows effective and fast spatiotemporal comparisons of CGT variation along cloud top pressure and seasonal partitioning of the data. We have used four years of the Pathfinder Atmospheres-Extended (PATMOS-x) data set [*Heidinger et al.*, 2014a] (derived from the passive satellite sensor AVHRR) to apply the method and to analyze the global distribution of the CGT from the results obtained.

The remainder of the paper is structured in the following way: the next section presents the methods, including the proposed model for CGT estimation and the EA used in this paper, with details on encoding and evolutionary operators considered. Section 3 describes the passive satellite data used in this work and the pre-processing steps carried out. Section 4 presents the results obtained for the global and seasonal distribution of CGT. Section 5 discusses physical explanations for the CGT behavior, as well as similarities and differences to previous studies. Section 6 provides a summary and indicates directions for future research.

2. Methods

2.1. CGT Estimation Model

The CGT is a complex parameter which depends on multiple factors such as dynamical properties of the cloud and the concentration of ice nucleating aerosol particles. In a small cloud volume, the supercooled liquid cloud water (mass) fraction ($\frac{q_l}{q_l+q_i}$, where q_l stands for the cloud liquid mixing ratio and q_i for the cloud ice mixing ratio) mostly occurs with values of close to 0 or close to 1, as shown by *Korolev et al.* [2003] from in situ sampling with averaging lengths on the order of 100 m. The liquid mass fraction can possibly assume intermediate values due to averaging of cloud heterogeneity on the scales of kilometers. However, the satellite retrieval used in this study provides only a binary liquid/ice information for pixels of 1×4 km^2 size. The liquid mass fraction distribution can thus be represented as a step function $U(T - T_g)$, where T stands for the variable (temperature) and T_g is the CGT under the cloud's conditions. This way, a cloud is in form of ice if $T < T_g$, whereas the cloud is in liquid form when $T > T_g$.

The value of T_g is not identical for all clouds. In fact, we could describe T_g as a Gaussian random variable, with a mean value T_{gm}, and variance $\sigma_g{}^2$. This model implies that the majority of clouds in a given region have CGT values similar to T_{gm}, but they can shift from this value with a given probability. This allows a simple statistical treatment for the CGT estimation from satellite images: consider a cloud with a given sampled cloud top temperature T_S. The probability that this cloud is in liquid phase is equal to the probability of $T_S > T_g$ with the (unknown) T_g of this cloud. As T_g is assumed to follow the Gaussian distribution with mean T_{gm} and variance $\sigma_g{}^2$, this probability can be calculated by the integral over this distribution from $T = -\infty$ to $T = T_S$:

$$P(w|T = T_S) = \int_{-\infty}^{T_S} (1/\sigma_g \sqrt{2\pi}) \cdot e^{\left(-\frac{1}{2}\left(\frac{T-T_{gm}}{\sigma_g}\right)^2\right)} \mathrm{d}T. \qquad (1)$$
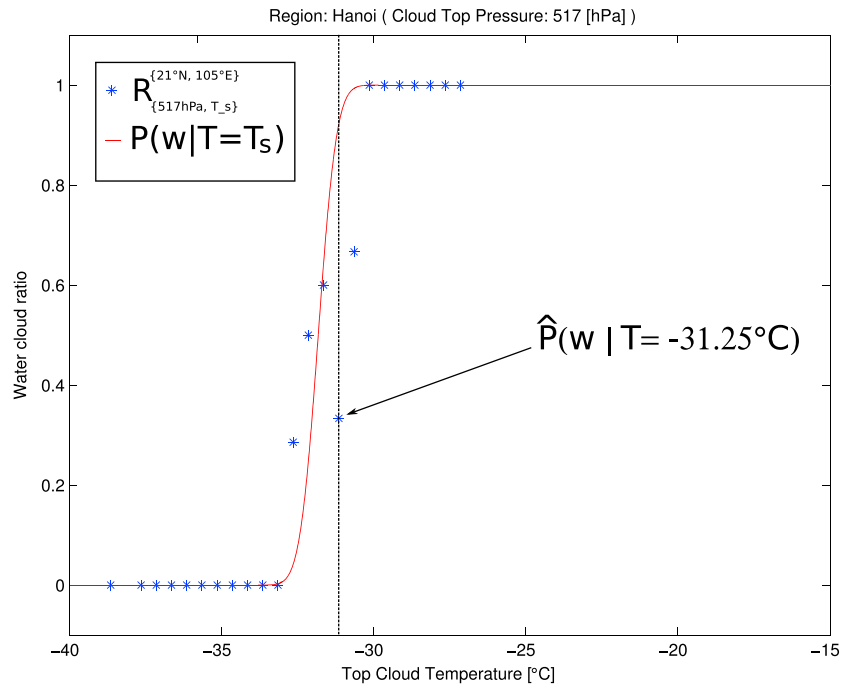
Figure 1. Example for the calculation of $\hat{P}(w|T = T_S)$ in a region over Hanoi (Vietnam).

Here $P(w|T = T_S)$ denotes the probability of the cloud top being in the liquid water (w) phase given that $T = T_S$. Note that from the satellite images we can estimate $P(w|T = T_S)$ for each temperature T_S by means of counting the pixels in liquid (N_w) and ice phase (N_i), and calculating the ratio $R = \frac{N_w}{N_w + N_i}$. Let $\hat{P}(w|T = T_S)$ be this estimation. The problem consists now of obtaining the σ_g and T_{gm} which best fits $\hat{P}(w|T = T_S)$ for the whole range of T_S in a given study zone (a horizontal box, e.g., of 10×10 pixels, and the full time series or seasonal subsets). Note that we can carry out this estimation for different cloud top pressure intervals in order to characterize the CGT for the different cloud types that appear in each pressure interval.

As an example for the calculation of $\hat{P}(w|T = T_S)$, Figure 1 shows a case in the region over Hanoi (Vietnam), for a cloud top pressure of 517 hPa. In this case the continuous red line stands for the cumulative distribution function $P(w|T = T_S)$ to be estimated. The observed values of R are shown as blue asterisks, which are used as $\hat{P}(w|T = T_S)$. In this example, the value of $\hat{P}(w|T = T_S)$ at $T_S = -31.25°C$ is approximately 0.3, while the estimated mean CGT for the selected area and cloud top pressure is $\approx -32°C$.

2.2. Evolutionary Algorithm

EAs are a family of bioinspired metaheuristics for solving optimization problems, based on mimicking the rules of natural evolution in a computer. There are many optimization problems which cannot be solved using classical approaches or standard computational methods due to its difficulty or intractability. In these cases where classical approaches fail, metaheuristic approaches have been shown as a possibility to obtain good enough solutions to the problem. Here the problem is to provide nonlinear best fits to the cumulative Gaussian distributions of the cloud top phase for large amounts of data. Here we solve the problem for the entire vertical column simultaneously, i.e., searching for the mean CGT T_{gm} and its standard deviation σ_g for all cloud top pressure intervals within the (horizontal and temporal) region of interest.

In EAs, the technique consists of encoding a reduced pool of candidate solutions (also known as *individuals* here: containing all vertical values of T_{gm} and σ_g in the region of interest) to the problem, forming a *population* ($\prod(\mathbf{x})$). This population of candidate solutions is then *evolved*, i.e., better solutions are obtained from the existing individuals in the current population, through the application of different evolution operators (operations over the current individuals to promote exploration of the search space and reaching the best possible solution). A pseudocode of an EA is given below:

Algorithm 1 General Evolutionary Algorithm (n_T)

1: $k \leftarrow n_T$

2: $InitializePopulation(\prod(\mathbf{x}))$

3: $Fitness(\prod(\mathbf{x}))$

4: **while** ($k > 0$) **do**

5:     $Selection(\prod(\mathbf{x}))$

6:     $Crossover(\prod(\mathbf{x}))$

7:     $Mutation(\prod(\mathbf{x}))$

8:     $Fitness(\prod(\mathbf{x}))$

9:     $k = k - 1$

10: **end while**

11: Return best individual $\mathbf{x}^*$ from $\prod(\mathbf{x})$

EAs are usually started by generating an initial population of individuals ($\prod(\mathbf{x})$), usually at random. In our problem of CGT estimation from satellite images, the problem's encoding in the EA is the following: each individual in the population is encoded as a vector $\mathbf{x} = \left[T_{gm}^1, \sigma_g^1, \ldots, T_{gm}^M, \sigma_g^M \right]$, where M stands for the number of cloud top pressure intervals considered (M is up to 200 pressure intervals in this study) for a given study zone. The initial values for the variables T_{gm}^l and σ_g^l (l stands here for the pressure interval index) are then obtained as follows: $T_{gm}^l = -33 + r$, where r is a random value in the range $(-10, 10)$ and σ_g^l is initialized as a uniform random value in $(0,1)$. The population size (number of candidate solutions in the population) is a parameter of the algorithm which has to be set prior to the initialization of the procedure. The population size must be small, so the computational complexity of the algorithm is kept low. In this case we use a population of only 50 individuals. After the population initialization, evolutionary operators are applied to each individual $\mathbf{x}$ in the population in a loop process. The algorithm is stopped after a predetermined number of generations (sequences of the loop, here chosen as $n_T = 5000$).

1. A selection operator aims at selecting those individuals that will be part of the population for the next generation. There are different possible implementations of the selection mechanism. For example, in roulette wheel selection, each individual has a probability of survival for the next generation proportional to its associated fitness value (objective function to optimize) [*Goldberg*, 1989]. Alternative selection mechanisms such as ranking selection and stochastic tournament are also possible [*Blickle and Thiele*, 1996]. In this paper we apply an stochastic tournament selection mechanism [*Yao et al.*, 1999], which has been reported to provide good results as selection operator. Tournament selection consists of performing selected comparisons between individuals (so called tournaments), in such a way that the best individual in terms of the objective function receives a "win" after each comparison. The parents of the next generation will consist of the individuals with most number of wins after the tournament procedures.

2. The crossover operator is applied in order to generate novel individuals from existing pairs of individuals in the population. In the standard implementation, individuals are paired at random, and cross (exchange parts of the binary string) is applied. Each pair then leads to another pair of individuals offspring, which may replace parents in the next generation (depending on the selection procedure applied). There are different types of crossover methods: one-point two-point or multipoint crossover, depending on whether the parents are crossed exchanging parts in one, two, or more points in the individual. Figure 2 shows an example of the two-point crossover operator used in this work.

3. Finally, the mutation operator is applied. Mutation causes changes in certain individuals of the population, with a very low probability. These changes help the algorithm escape from local optima when it is stuck during evolution. There are several possibilities to implement this operator, such as obtaining the changes in the individuals using different types of probability density functions (uniform, Gaussian, etc.). In this paper we use Gaussian mutations to introduce random changes both in T_{gm}^l and σ_g^l components of $\mathbf{x}$.
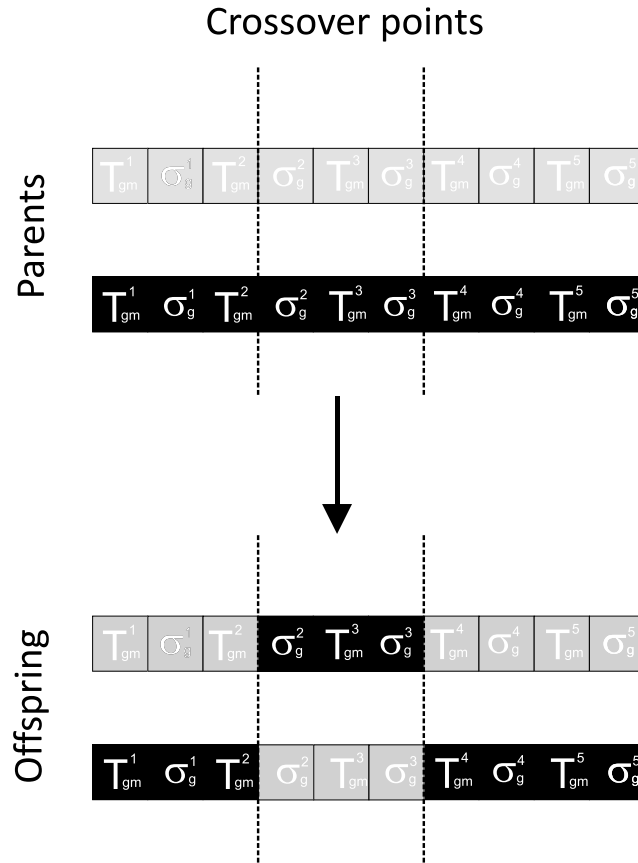
Figure 2. Example of a two-point crossover operator in an evolutionary algorithm.

Specifically, $(T^l_{gm})_{mut} = T^l_{gm} + 3 \cdot G(0, 1)$, where $(T^l_{gm})_{mut}$ stands for the mutated value of T^l_{gm}, and $G(0, 1)$ is a Gaussian mutation of mean 0 and variance 1. Note that the final variance for this mutation is 3. In the case of σ^l_g, the mutation is carried out as $(\sigma^l_g)_{mut} = \sigma^l_g + 0.3 \cdot G(0, 1)$.

The objective function to be minimized by the EA is given by the mean square error (mse) between $P(w|T = T_S)$ and $\hat{P}(w|T = T_S)$ as a sum over all levels, since this process is more efficient than applying it to each level individually. The final form of the objective function is then

$$\text{mse}(\mathbf{x}) = \sum_{n=1}^{N} \sum_{l=1}^{M} \left(P_{\sigma^l_g, T^l_{gm}} \left(w|T_n = T_S \right) - \hat{P}^l \left(w|T_n = T_S \right) \right)^2. \quad (2)$$

The summation over index n integrates over all (N) temperature bins (0.5 K intervals).

3. Data Set Description

The CGT estimation is applied to the cloud product of the PATMOS-x AVHRR cloud and climate data set [*Heidinger et al.*, 2014a]. This data set has the advantages of providing a high spatial resolution, a long-term, homogenized record, a gridded, easily manageable data format and an advanced cloud type and phase retrieval. However, as it is based on passive satellite sensors with a limited number of spectral channels, the retrieval of cloud microphysical properties will include ambiguities and perform less well than active sensors. With active sensors, a global study as shown here would not have been possible because of the sparseness of the data. While we identify some potential weaknesses of the PATMOS-x cloud phase and cloud top temperature data, further improvements of the retrievals are beyond the scope of this study.

PATMOS-x is based on measurements by the AVHRR sensor on board 14 different NOAA (National Oceanic and Atmospheric Administration) and European Organisation for the Exploitation of Meteorological Satellites polar orbiting satellites, covering 1979 to present (Table 1). The spatial resolution of the AVHRR global area

Table 1. Satellites Contributing to the PATMOS-x Data Set as in *Heidinger et al.* [2014a][a]

Satellite Name	Start Date	End Date
TIROS-N	01/01/1979	01/19/1980
NOAA-06	06/30/1980	08/19/1981
NOAA-07	08/24/1981	02/01/1985
NOAA-08	05/16/1983	10/13/1985
NOAA-09	02/25/1985	11/06/1988
NOAA-10	11/17/1987	09/16/1990
NOAA-11	11/08/1988	08/31/1994
NOAA-12	09/16/1991	12/14/1998
NOAA-14	02/09/1995	07/25/2002
NOAA-15	10/26/1998	05/06/2016
NOAA-16	03/20/2001	07/19/2006
NOAA-17	08/24/2002	01/10/2009
NOAA-18	07/19/2005	05/06/2016
METOP-02	06/29/2007	05/06/2016
NOAA-19	04/19/2009	05/06/2016

[a]Data from satellites in boldface are considered in this study for the period 1 June 2009 to 31 May 2013 (all dates in month/day/year format).

coverage (GAC) pixels is approximately 1×4 km^2, but they are subsampled without any averaging onto a $0.1° \times 0.1°$ regular grid (level-2b data) with two values per day, collecting all ascending and descending overpasses [*Heidinger et al.*, 2014a]. PATMOS-x provides a seven-level cloud-type specification (fog, water, supercooled water, opaque ice, cirrus, overlapping (multilayer), and overshooting clouds) based on measurements at four wavelengths (0.65, 1.6/3.75, 10.8, and 12.0 μm), to which brightness temperature difference tests and reflectance thresholds are applied [*Pavolonis et al.*, 2005]. As in *Heidinger and Pavolonis* [2009], we treat the fog, water, and supercooled water as liquid water clouds, while the others are treated as ice clouds. The cloud top temperature is derived from split-window observations (at 10.8 and 12.0 μm) by an optimal estimation approach [*Heidinger and Pavolonis*, 2009], which gives consistent results for day and night overpasses. The third variable used in this study, the PATMOS-x cloud top pressure, is derived [*Heidinger and Pavolonis*, 2009] by locating the cloud top temperature within the temperature profile of the National Centers for Environmental Prediction (NCEP) Climate Forecast System Reanalysis [*Saha et al.*, 2010]. The PATMOS-x cloud observations have been evaluated against other long-term records of clouds [*Stubenrauch et al.*, 2013] using monthly mean fields. *Stengel et al.* [2015] performed a pixel-based validation of cloud phase and cloud top temperature for different AVHRR retrieval schemes against CALIOP. The PATMOS-x retrieval [*Pavolonis et al.*, 2005] performed best among the tested schemes, with a probability of correct detection of ice clouds of 89% and a probability of detection of liquid clouds of 88%. Furthermore, the cloud top height compared best with CALIOP, indicating a good quality of the PATMOS-x cloud top pressure and cloud top temperature data.

In this study, four full years of PATMOS-x data [*Heidinger et al.*, 2014b] are analyzed, merging the information from the NOAA-18, NOAA-19, and METOP-2 satellites from 1 June 2009 to 31 May 2013 (see Table 1). This time span has been chosen because it includes overlapping data from the newest AVHRR instruments (AVHRR/3), which are assumed to be most accurate. Thus, we can use six daily overpasses (one midmorning and two afternoon satellites). Figure 3 shows two-dimensional histograms of the ice and liquid water pixels from the full 4 years of data and all grid points. For this and the following analyses, bin sizes of 0.5°C and 5.5 hPa are used. Ice clouds (Figure 3a) are detected primarily above 700 hPa, with most cloud top temperatures between −20 and −80°C. A small number of ice cloud pixels close to the surface with derived cloud top temperatures above 0°C seem to be erroneous retrievals. Liquid water clouds (Figure 3b) occur with cloud top temperatures mainly between −30 and +30°C, at altitudes between 1000 and 300 hPa. Also here, some artifacts can be identified: cloud top pressures above 1050 hPa seem to be unrealistic, as well as liquid clouds with cloud top temperatures above −20°C at altitudes above 500 hPa. Furthermore, the frequency of liquid water clouds shows discontinuities at −20°C and 0°C, which might be due to reclassification tests in the retrieval scheme. The horizontal stripes in the histograms originate mostly from grid points over ice-covered surfaces at the high latitudes and may be due to discrete model levels of the reanalysis profiles used in PATMOS-x In the following, all cloud top temperature/pressure bins with less than 500 cloudy pixels are excluded from the analysis, which excludes most of these obviously problematic regions. Figure 3c shows the ratio of liquid water to all clouds (R). The region of interest for this study is the transition zone from 0 to 1, in which the CGT is diagnosed by the EA described above. For this, the data are aggregated into boxes of 10×10 level 2b grid cells (i.e., $1° \times 1°$) for the regional distribution of CGT and into zonal bands of 1° for the calculations of zonal average CGT, such that enough data (for the $1° \times 1°$ boxes, depending on the cloud cover, up to 100 values 6 times per day for 4 years) are available to generate the cumulative distribution for the chosen cloud top pressure intervals of 5.5 hPa, as shown in Figure 1. In order to focus on the transition zones, for each box, we only consider the
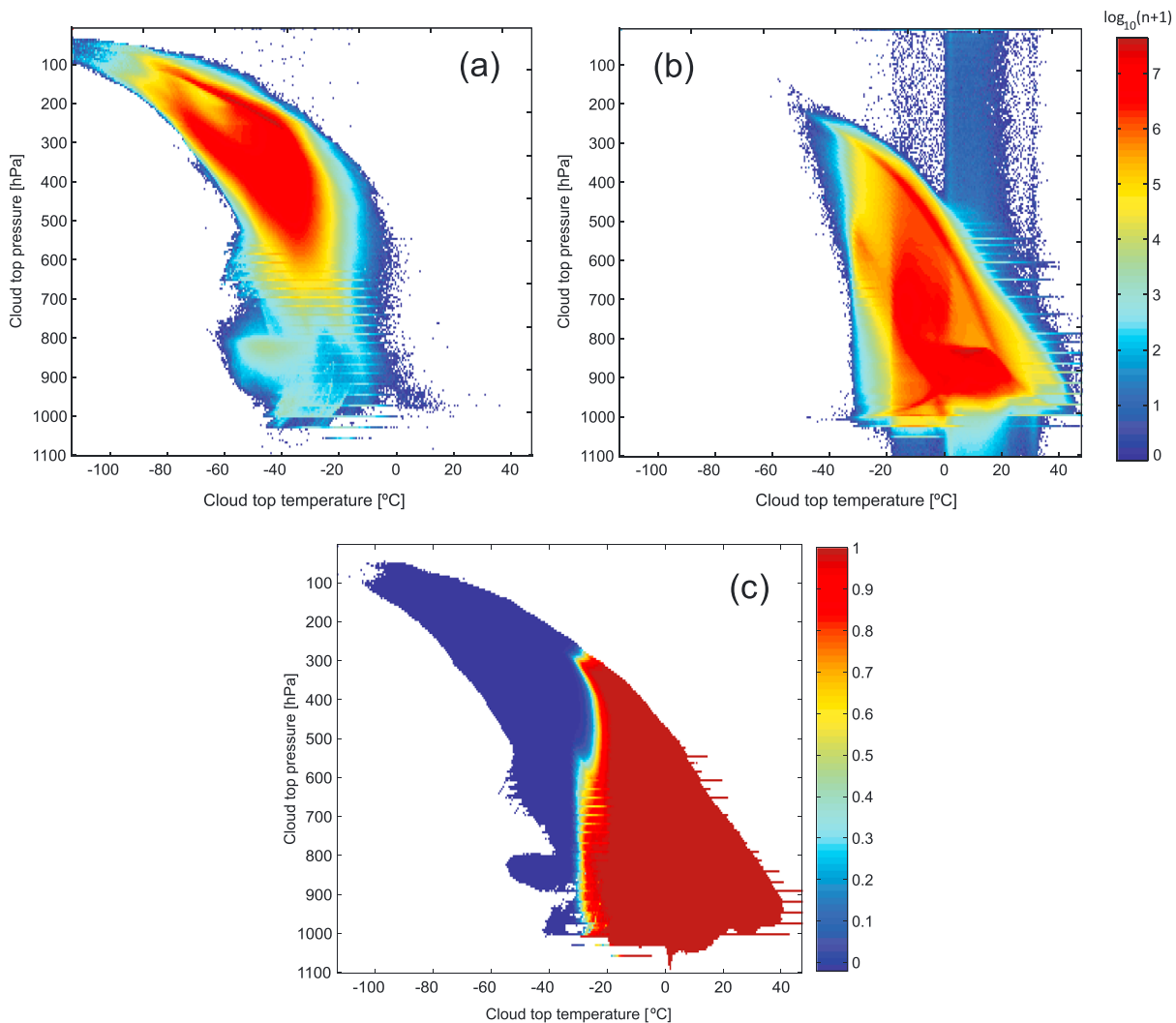
Figure 3. Two-dimensional histograms of the number of pixels per (0.5°C × 5.5 hPa) bin (*n*) of (a) ice and (b) liquid water clouds as a function of cloud top pressure and cloud top temperature, and (c) ratio of liquid water to all the clouds (liquid plus ice clouds). A filter has been applied in Figure 3c to remove all bins with less than 500 cloudy pixels.

cloud top pressure intervals that contain at least one value of $R > 0.5$ and also at least one value $R < 0.5$. Note that this way we discard all cloud top pressure intervals where there are not enough water or ice clouds.

4. Results

4.1. Variation of the CGT

The zonal mean CGTs are displayed in Figure 4 as a function of cloud top pressure for the four seasons (DJF: December–February, MAM: March–May, JJA: June–August, and SON: September–November). Figure 5 displays global maps of the annual mean CGT in different cloud top pressure intervals. No data are shown where CGT cannot be calculated due to too few water and ice clouds at the same cloud top pressure and temperature interval. Note that the polar latitudes (90°S to 72°S and 72°N to 90°N) will be disregarded in the following discussion due to the uncertainties in the cloud retrieval over ice-covered surfaces [*Xiong et al.*, 2002]. A consistent feature in all four seasons is the low value of the CGT in the tropical upper troposphere. Here the CGT reaches down to −38°C, approximately the homogeneous freezing threshold. This is probably linked to the strong convection in this region and the retention of liquid water due to the vigorous updrafts. There is also a narrow vertical region of low CGT at the top of the mixed-phase cloud region at almost any latitude and season, indicating that some (infrequent) strong convective events can result in strongly super-cooled liquid water also outside the tropics. The decrease of CGT with altitude at these temperatures follows
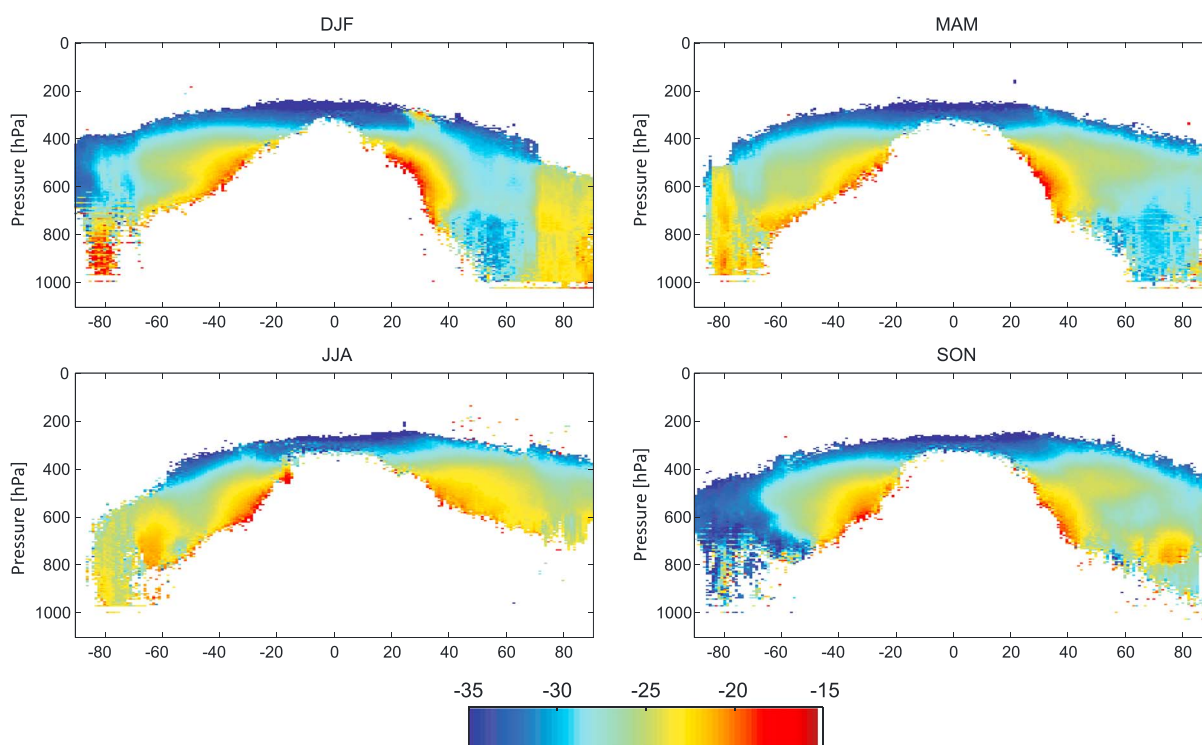
Figure 4. Seasonal zonal mean CGT in °C as a function of latitude and cloud top pressure.

the annual average ambient temperature profile, which varies little in this region: the higher any supercooled water is lifted, the colder it has to be (while the majority of clouds will be frozen at these altitudes).

In the subtropics, high CGT values around −20°C are found between 700 and 450 hPa. In the Northern Hemisphere summer, this feature extends to the pole, although the highest zonal mean CGTs (−15°C) are found at low latitudes and the lowermost cloud top pressure intervals where data can be evaluated. The latter is expected from the ambient temperature gradient, but it is obvious from these figures that subtropical clouds have a tendency to freeze at higher temperatures than clouds at other locations. As can be seen in Figure 5 for the cloud top pressure intervals 553–558 hPa and 608–613 hPa, the highest CGTs in the midlatitudes are found over ocean, in particular, of the western North Pacific and the western North Atlantic. In these regions, there is about 10 K difference in CGT to the adjacent continental regions, which exhibit lower CGTs. The land-sea difference will be discussed further below. In Figure 5, the major mountain ranges (e.g., the Himalayas or the Rocky Mountains) stand out with lower CGTs than the surrounding areas. This may be due to the different nature of the clouds in the boundary layer over mountainous terrain than in the free troposphere at the same cloud top pressure.

The Northern Hemisphere middle and high latitudes exhibit a distinct seasonal cycle, with CGTs above −25°C at all altitudes except for the tropopause region in summer (June–August (JJA)), but CGTs around −30°C at midlatitudes in winter (December–February (DJF)), and at middle and high latitudes in winter and spring (DJF and March–May (MAM)). In MAM and to some extent also in DJF and September–November (SON), the CGT has a broad maximum around 500 hPa, with lower values both above and below. The Northern Hemisphere fall (SON) is an exception with a secondary maximum of CGT between 60 and 80°N and 800 and 600 hPa. However, this maximum is linked to high CGT values over Greenland (see Figure 5, 663–668 hPa), where the cloud retrieval may be affected by the snow and ice-covered surface.

The decrease of the CGT to lower values in the lower troposphere (below approximately 700 hPa) is remarkable, as the mean ambient temperature always decreases with altitude. This means that in the lower troposphere, clouds only transition from liquid to ice if the temperatures are much lower than average. So here only a small subset of all clouds undergoes a phase transition, while the majority of all clouds remains liquid. The concentration of ice nucleating particles is highest close to the surface sources, but this does not
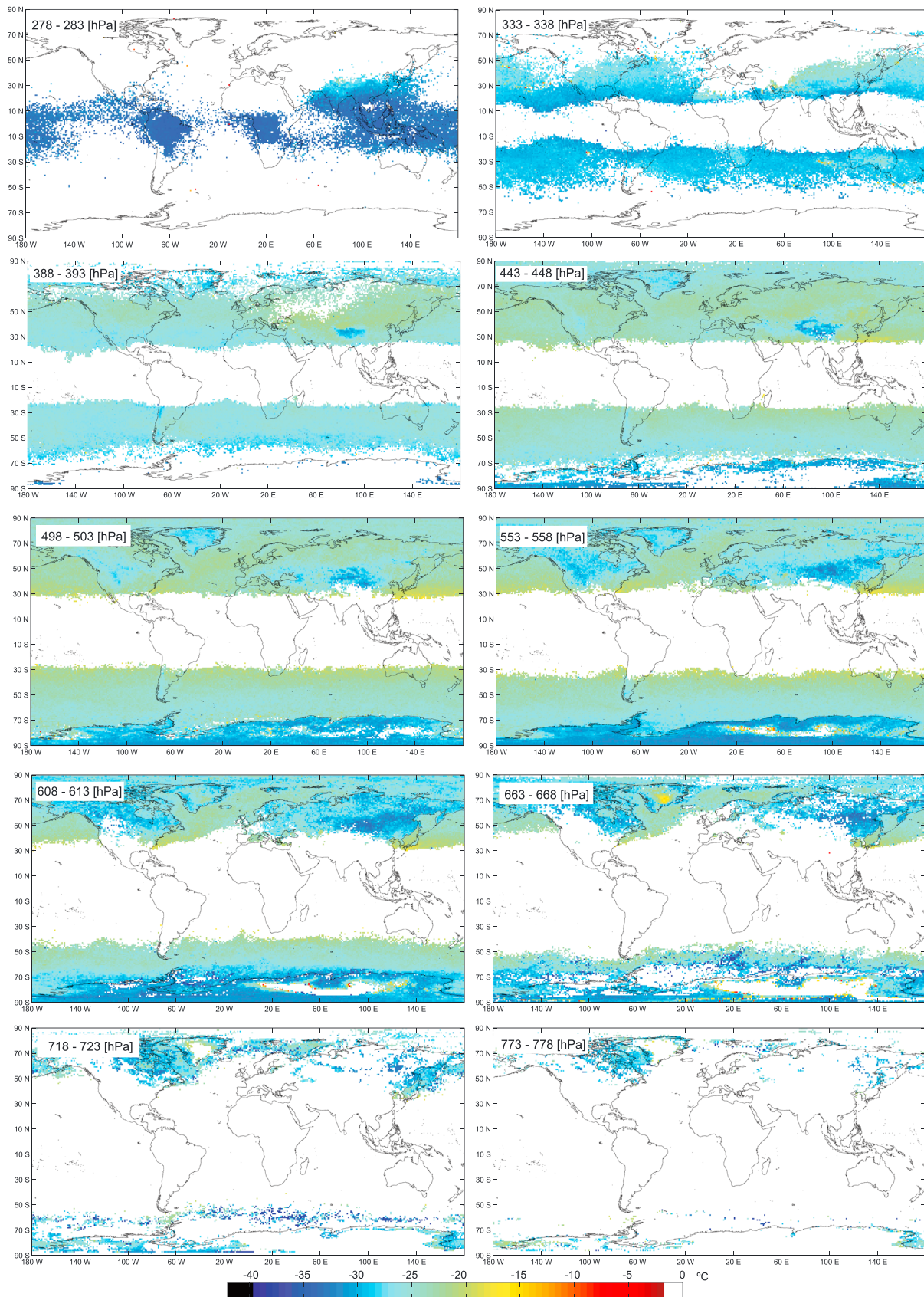
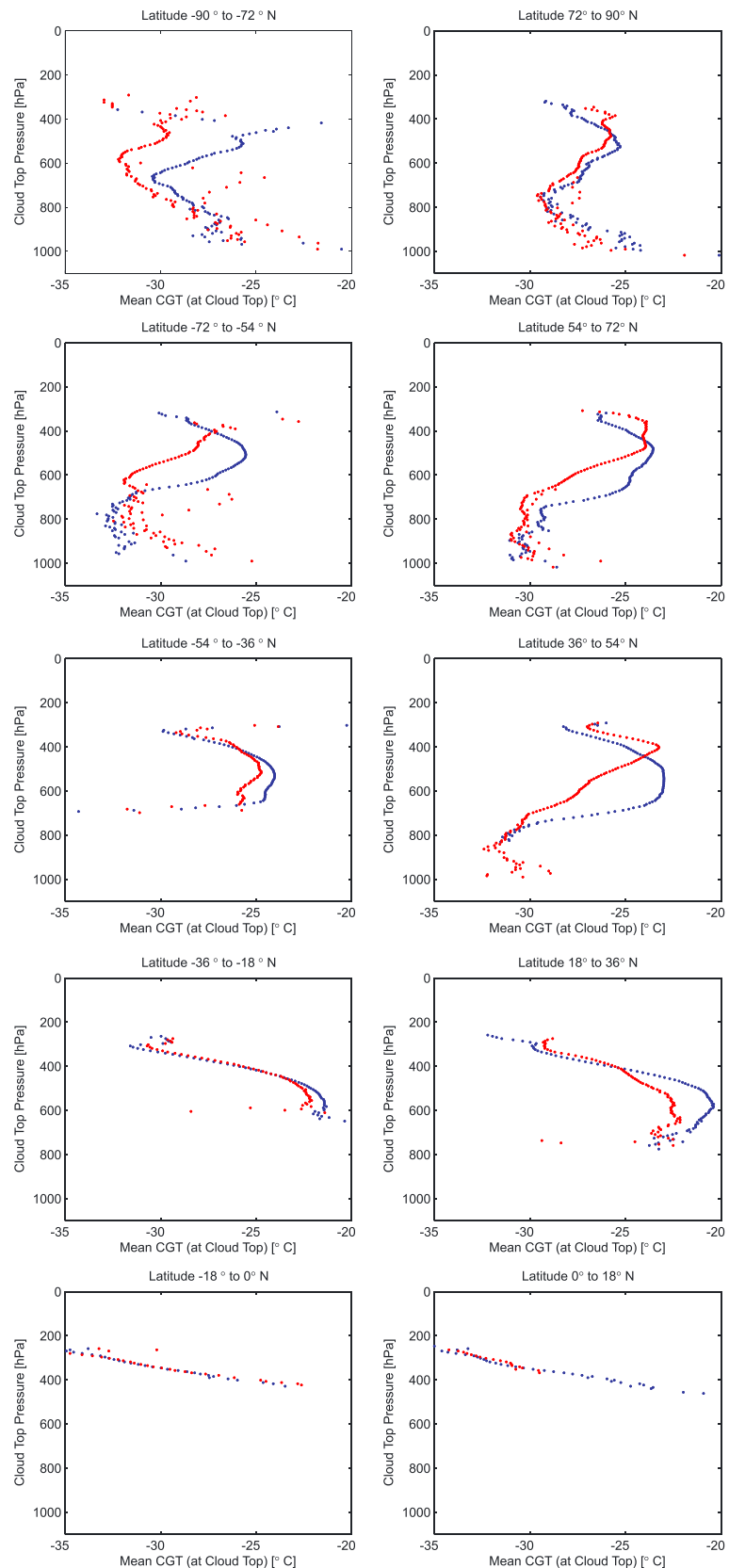**Figure 5.** Annual mean CGT for different cloud top pressure intervals.

Figure 6. Vertical profiles of the annual mean CGT for different latitude bands. Blue dots represent values over sea, whereas red dots represent values over land.
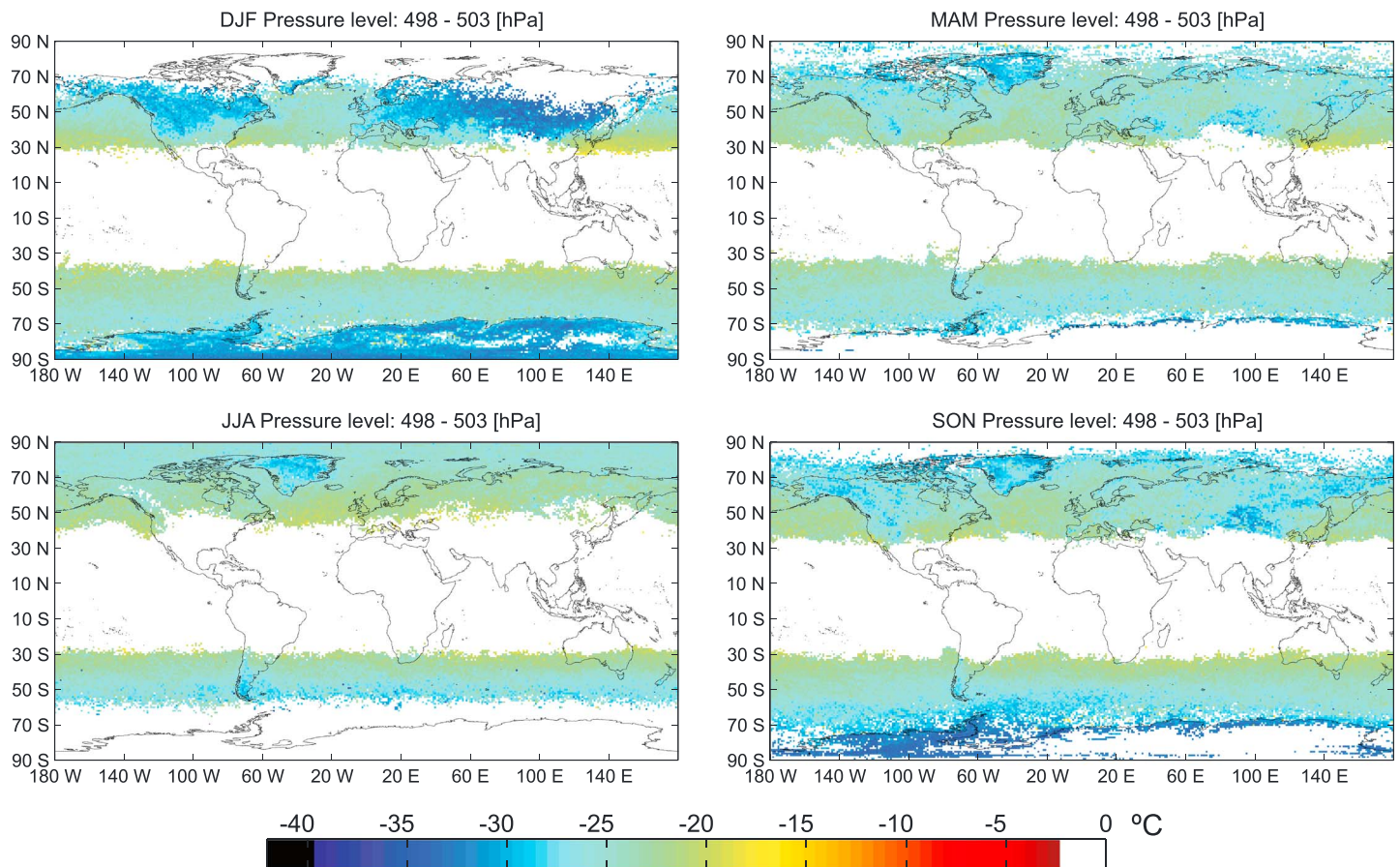
Figure 7. Seasonal CGT for a cloud top pressure interval of 498–503 hPa.

seem to have a significant effect on the estimated CGT. The observed effect could be linked to the efficiency of secondary ice mechanisms: low clouds contain typically less liquid water and smaller hydrometeors than clouds extending to middle and high levels, while suggested ice multiplication via the Hallett-Mossop mechanism [*Hallett and Mossop*, 1974] requires the presence of large droplets.

Vertical profiles of the CGT are displayed in Figure 6, segregated into pixels over land and over ocean. Close to the equator, the CGT shows a monotonic decrease in the upper troposphere. In the subtropics and midlatitudes, the maximum in the midtroposphere as described above is clearly visible in the vertical profiles. The maximum tends to be reached at higher altitudes over land than over ocean (see, e.g., 36°N to 54°N in Figure 6), such that the CGT is higher over ocean than over land between 800 and 500 hPa at most latitudes. This might be counterintuitive due to the expectation of higher concentrations of ice nucleating particles over land. In the seasonal variation of the global CGT distribution at 498–503 hPa (Figure 7), it can however be seen that the land-sea contrast at these altitudes is strongest in the winter months (DJF for the Northern Hemisphere and JJA for the Southern Hemisphere) and nearly disappears in summer. From Figure 6 (second and third rows) it is also evident that in the middle and high latitudes, marine clouds in the Southern Hemisphere have lower CGTs than their Northern Hemisphere counterparts.

Finally, the variance of the CGT (Figure 8) is lowest in the tropics and highest at high latitudes. In the middle/upper troposphere and in most latitudinal bands, the variance is higher over land than over ocean. This could be an indication of the stronger diurnal, seasonal, synoptic, and/or aerosol-induced variation in the CGT over land.

4.2. Limitation of the CGT estimation
In Figure 9, the mean CGT for the Northern Hemisphere winter (DJF) at 338–344 hPa is shown. In a region around 30°N extending from the Indian subcontinent across the East China Sea and the North Pacific, CGTs
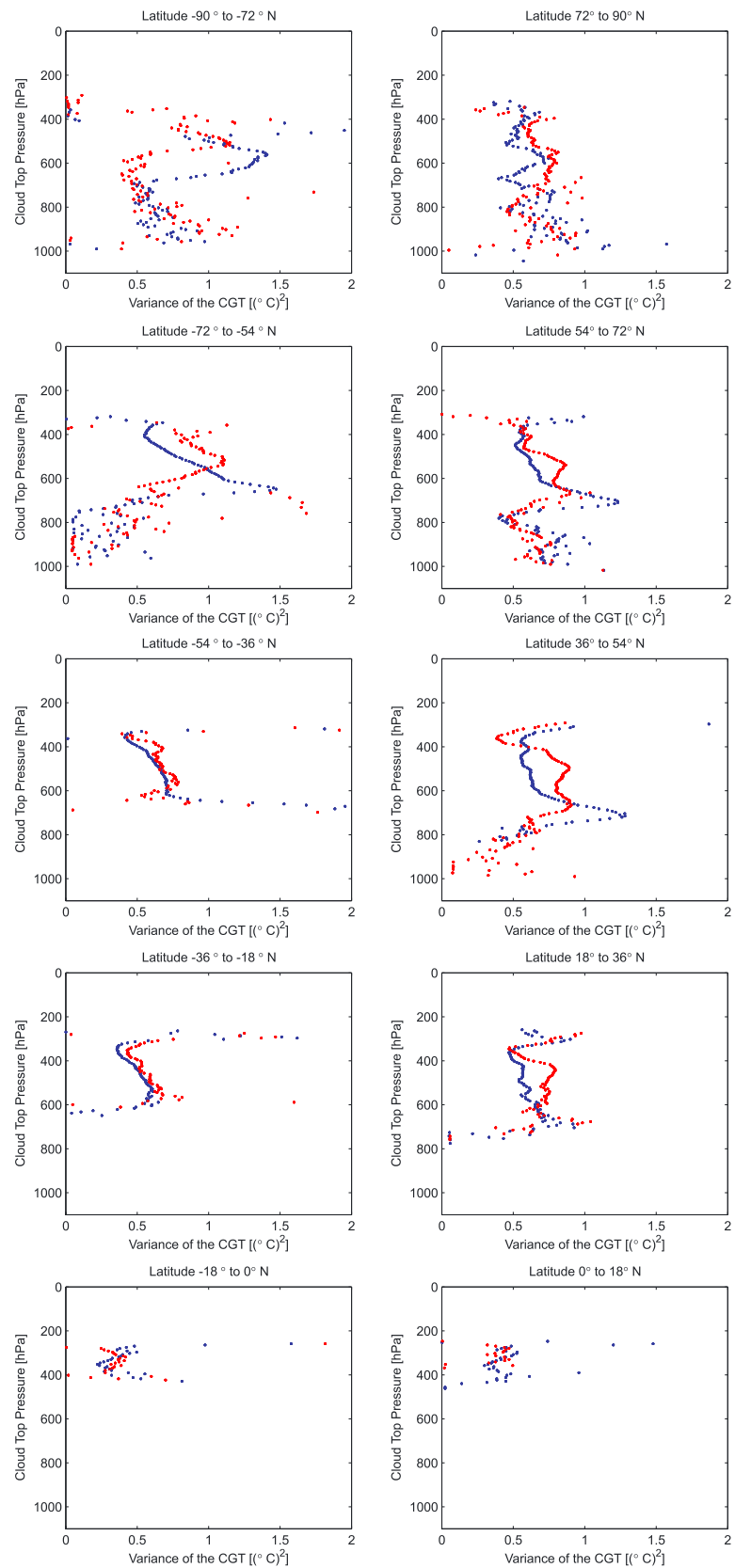
Figure 8. Vertical profiles of the annual CGT variance (σ_g^2 in (°C)^2) for different latitude bands. Blue dots represent values over sea, whereas red dots represent values over land.
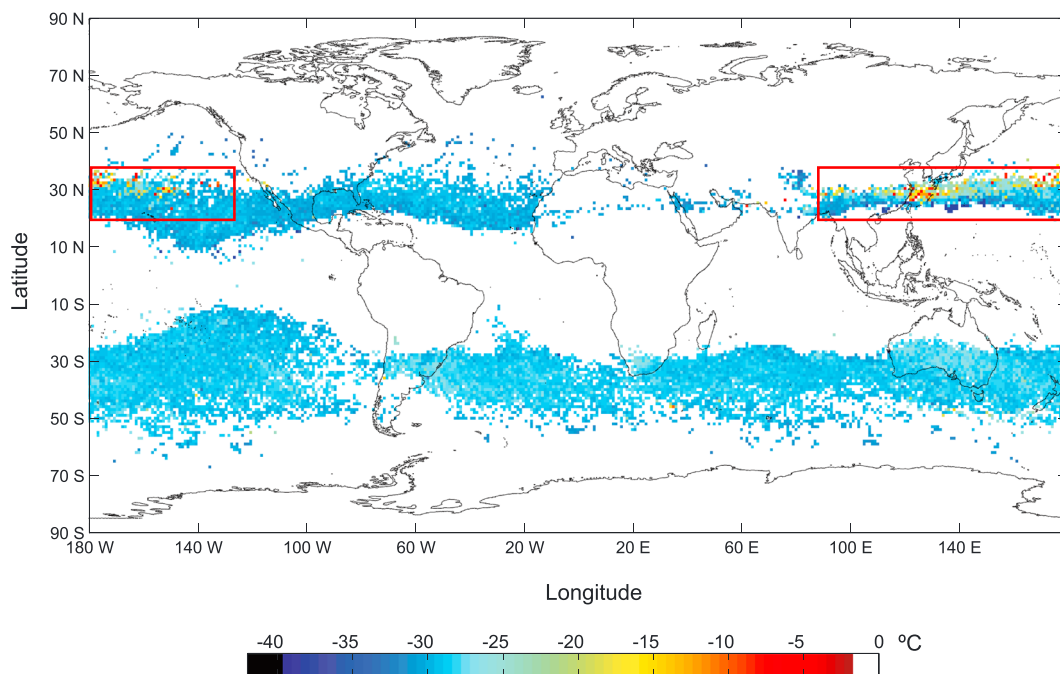
Figure 9. Annual mean CGT for the cloud top pressure interval 338–344 hPa in December, January, and February. The red box includes the data points further analyzed in Figure 10.

above −20°C are derived. This feature is only found in winter and not in the other seasons, as can be seen in the zonal average (Figure 4). The two-dimensional distributions of the distribution of the liquid water cloud ratio *R* (Figure 10) indicate a clearly different behavior of *R* in winter compared to summer. In summer (Figure 10a), *R* always decreases with decreasing temperature at all cloud top pressures. In winter, however (Figure 10b), at pressures lower than approximately 350 hPa, *R* remains constant or even shows a bimodal behavior as a function of temperature. In this case, the proposed CGT estimation model (based on the assumption of a cumulative Gaussian distribution of *R*) is no longer valid, and the EA may be locked into a local minimum and may fail to produce a correct value of CGT and its variance. Nevertheless, the high values of CGT in Figure 9 are the result of the unusual behavior of clouds in this region which may be real. The two-dimensional distribution of *R* (Figure 10b) implies the presence of unusually warm ice clouds in this region.
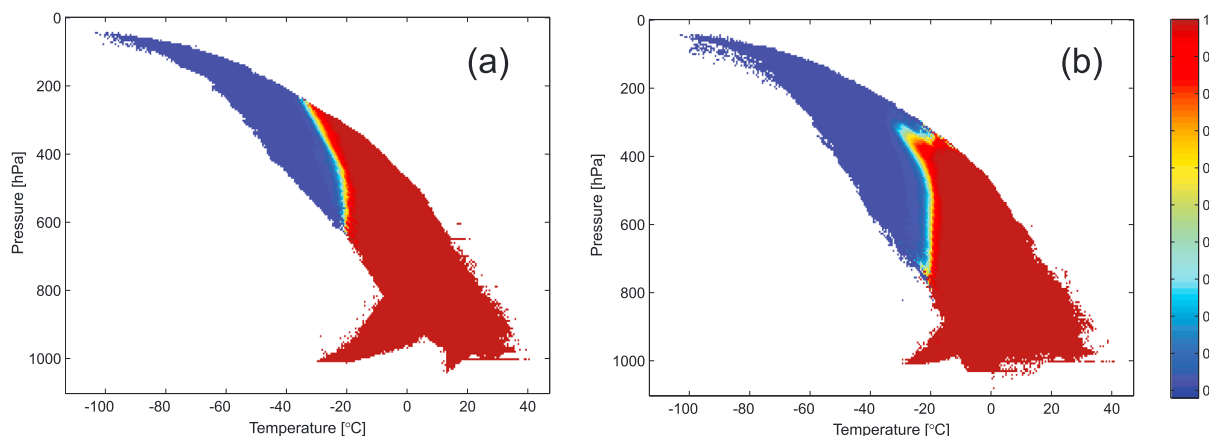

Figure 10. Ratio of liquid water to all the clouds (liquid plus ice clouds) for the region marked in Figure 9. (a) summer: June, July, and August and (b) winter: December, January, and February.

5. Discussion

The vertical variation of the CGT allows new insights compared to previously presented two-dimensional (horizontal) analyses of the cloud top phase distribution. In particular, evidence for a dominance of homogeneous freezing in the top layers of deep convective clouds in the tropics, but also in the subtropics and midlatitudes in the upper troposphere, can be inferred from the low values of CGT in these regions. This agrees with numerical simulations of deep convective clouds [e.g., *Phillips et al.*, 2005; *Fan et al.*, 2010]. The reasons for the broad maximum of the CGT in the midtroposphere are not fully understood, but we suggest that it can be linked both to dynamical effects (less vigorous updrafts in the alto clouds which exist in these altitudes [*Larson et al.*, 2006]) and to microphysical effects (higher concentrations of ice nucleating particles, larger droplets, and thus more efficient secondary ice production). Toward lower altitudes, the estimated CGT decreases again at all latitudes except for the tropics. For lower altitudes, fewer and fewer ice clouds are detected (see Figure 3a), partly because low clouds which are obscured by midlevel, and high clouds are not seen by passive remote sensing from space and are not represented in PATMOS-x. An analysis of CALIOP observations (not shown) indicates that about half of all low clouds occur below upper level clouds. It may be that the decrease in CGT is due to the fact that these clouds are missing in the analyzed data. However, the decrease in CGT at lower altitudes is confirmed by the CALIOP-based analysis of the supercooled liquid cloud fraction presented by *Hu et al.* [2010]. This effect could be due to the more frequent occurrence of clouds with liquid cloud tops above ice-dominated layers in the planetary boundary layer than at upper levels and to the limitation of our analysis to cloud top phase. In mixed-phase boundary layer clouds (e.g., Arctic stratocumulus), the cloud top often consists of a thin liquid layer, while ice can dominate within and below the cloud [e.g., *Morrison et al.*, 2012]. Therefore, these clouds only glaciate when the concentrations of ice nucleating particles and ice crystals are relatively high [*Paukert and Hoose*, 2014]. A similar vertical phase distribution can exist in midlevel altocumulus clouds [*Fleishauer et al.*, 2002], but other clouds with stronger updrafts can also exist at these levels, in which ice particles can remain suspended in the cloud top region.

Southern Hemispheric marine clouds have been described to contain large amounts of supercooled liquid water [*Morrison et al.*, 2011; *Chubb et al.*, 2013]. Our study confirms that they have a lower average CGTs than marine clouds at the same latitudes in the Northern Hemisphere. The zonal and annual average distribution of the CGT, however, shows little hemispheric difference due to the asymmetry in the distribution of the continents.

The analysis of the mean CGT profiles reveals a distinct land-sea contrast at cloud top pressures between approximately 400 and 800 hPa, with higher values of CGT over ocean than over land. In the lower troposphere, this effect may be due to the lower cloud top pressures at the boundary layer inversion above orography (due to the height of the underlying orography and to the often deeper boundary layers over land). However, this does not explain the difference at upper levels. The sign of the land-sea contrast in CGT agrees with the early global study of *Giraud et al.* [2001], who created a 1 day average cloud phase distribution between 60°N and 60°S. Also, *Rosenfeld et al.* [2011] reported higher CGTs for maritime clouds than for continental ones when analyzing 147 convective clouds over East Asia and the West Pacific. They could show that the high CGT is linked to large droplet radii and argued that this hinted at an efficient ice multiplication mechanism operating in these clouds. It is remarkable that we find very similar CGTs over ocean in the same region. In contrast, *Hu et al.* [2010] derived a higher global average CGT over land than over ocean from CALIOP nighttime observations. This difference could be due to the diurnal cycle of convection. Segregating the data into convective/stratiform regimes by using vertical velocity or stability as indicators could help to identify the reasons for this discrepancy. In addition, *Naud and Kahn* [2015] reported more ice clouds over land than over ocean for a given cloud top temperature in their analysis of winter extratropical cyclones. In winter, we find the most pronounced land-sea difference in the midtropospheric CGT, but with lower values of CGT over land. This disagreement could be due to the subsampling by *Naud and Kahn* [2015] for the specific synoptic situation they analyzed. Compared to the analysis of the supercooled liquid cloud fraction from CALIOP [*Choi et al.*, 2010b; *Komurcu et al.*, 2014] at an isotherm of −20°C, partial agreement and partial disagreement is found. While *Choi et al.* [2010b] reported higher values of the supercooled liquid fraction over ocean than over land, which translates into lower CGTs over oceans and thus the opposite of our findings, the analysis of a longer record of CALIOP data shown in *Komurcu et al.* [2014] reported less clear land-sea differences, including the opposite trend than *Choi et al.* [2010b] for the North Pacific compared to adjacent continents. How much of the difference between our results and the CALIOP studies is due to the ability of CALIOP to distinguish liquid water and ice not only at the cloud top but also within (optically thin) clouds, is beyond the scope of

this study. *Choi et al.* [2010b] suggested that the supercooled liquid cloud fraction is negatively correlated with the frequency of occurrence of dust aerosols, which originate from continental sources. However, vertical velocity, cloud thickness and humidity also impact cloud glaciation, such that the aerosol effect is difficult to isolate. Furthermore, also, oceans emit ice nucleating particles [*Wilson et al.*, 2015], and secondary ice production is assumed to be most efficient in the presence of large droplets, which are more likely to occur in marine clouds [*Lawson et al.*, 2015]. If there was a dominant impact of continental aerosols on cloud glaciation, we would expect this effect to be visible in all remote sensing data sets, including ours. The absence of this signal suggests that other microphysical processes, cloud dynamical effects, and retrieval characteristics are at least equally important as effects of continental aerosols.

We presume that the unusually high CGT values in a region around 30°N and above 350 hPa are real, because there are no particular reasons for retrieval errors (such as ice-covered surfaces) in this area. From a closer inspection of some of the relevant cloud scenes (not shown), the warm ice clouds appeared to occur in stratiform cloud systems, such as warm conveyor belts. In the West North Pacific, such systems occur more often in winter than in summer [*Madonna et al.*, 2014] and transport air masses from the lower to the upper troposphere. We can speculate that this entails the transport of ice nucleating aerosol particles. Alternatively, some special dynamical features in the clouds could lead to their early glaciation. The further analysis of the reasons for this behavior will be the topic of future studies.

While PATMOS-x is a mature data set, we assume that some uncertainty may be introduced into our analysis by unavoidable limitations of the AVHRR sensor and retrieval shortcomings. For example, misclassification of the cloud phase could potentially impact our analysis. However, the analysis by *Stengel et al.* [2015] indicates a nearly bias-free cloud phase product in PATMOS-x compared to CALIOP; thus, the determination of the CGT as presented in this paper is likely to be affected only to a small degree by this. Errors in the PATMOS-x cloud top height assignment could have impacted our analysis as well. Since cloud top height is underestimated by PATMOS-x on average when compared against CALIOP [*Stengel et al.*, 2015], it is no unlikely that the results in our study are also biased in that respect, meaning that information is assigned to an atmospheric layer but rather belongs to layers above. Since the underestimation might be more significant for ice clouds, one could speculate that when analyzing individual atmospheric layers an ice bias was introduced, which could potentially bias the derived CGT to higher values.

Furthermore, three AVHRR-related limitations shall be mentioned. First, due to the passive measurement procedure of AVHRR and its limited spectral information, very thin clouds are systematically missed by AVHRR [*Karlsson and Johansson*, 2013; *Stengel et al.*, 2015], because they have only a small impact on the measured radiation. Second, the PATMOS-x data set is based on AVHRR GAC pixels, which have a footprint size of approximately 1×4 km^2, which inhibits resolving clouds and cloud processes at spatial scales smaller than that. Third, once a cloud layer has a certain optical depth, no signal of cloud layers underneath can be detected. This means that potentially existing middle- and low-level clouds that are obscured by high-level clouds were not included in our study.

6. Summary

In this manuscript, an evolutionary algorithm has been developed to allow an efficient calculation of the CGT for a large gridded data set of cloud top properties from PATMOS-x. The CGT and its variance are calculated for boxes of $1° \times 1°$ and vertical layers of 5.5 hPa thickness. To our knowledge, this is the first analysis of the vertical variation of CGT from passive remote sensing data. We find that CGT as function of cloud top pressure exhibits a characteristic sickle shape. Lowest CGTs close to homogeneous freezing are found in the upper troposphere, while maximum values (between −20 and −25°C) are found in the midtroposphere. In the lower troposphere (below approximately 700 hPa), the derived CGT is significantly lower, but fewer data are available here due to relatively high average ambient temperatures and thus a low number of ice clouds. Data in the lower troposphere at high latitudes may be contaminated by signals from ice-covered surfaces. In most altitude and latitude areas, the annual mean CGT is higher over ocean than over land, primarily due to a difference in the winter months. The variance of CGT increases from the equator to the poles. In a few regions, in particular, above the West North Pacific, the estimation model fails because of a bimodal structure of the cloud phase distribution at specific cloud top pressure intervals.

Future studies should explore the reasons for the variation of CGT in combination with ancillary data, such as vertical velocity or stability (to quantify the convective or stratiform character of different cloud regimes)

and proxies for aerosol concentrations (aerosol optical depth). Furthermore, global aerosol models as well as field observations could help to constrain the global distribution of ice nucleating particles, and cloud models with advanced microphysics schemes could elucidate the relevance of primary and secondary ice formation as well as vertical transport for the cloud top phase distribution.

References

Ahn, J.-B., and J. Lee (2016), A new multimodel ensemble method using nonlinear genetic algorithm: An application to boreal winter surface air temperature and precipitation prediction, *J. Geophys. Res. Atmos.*, *121*, 9263–9277, doi:10.1002/2016JD025151.

Babb, D. M., J. Verlinde, and B. A. Albrecht (1999), Retrieval of cloud microphysical parameters from 94-GHz radar doppler power spectra, *J. Atmos. Oceanic Technol.*, *16*, 489–503.

Baum, B. A., W. P. Paul Menzel, R. A. Frey, D. C. Tobin, R. E. Holz, S. A. Ackerman, A. K. Heidinger, and P. Yang (2012), MODIS cloud-top property refinements for collection 6, *J. Appl. Meteorol. Climatol.*, *51*(6), 1145–1163.

Blickle, T., and L. Thiele (1996), A comparison of selection schemes used in evolutionary algorithms, *Evol. Comput.*, *4*(4), 361–394.

Bravy, B. G., G. K. Vasiliev, and V. Y. Agroskin (2002), Recognition of composition and of microphysical characteristics of aerosol clouds in multifrequency sounding, paper SPIE 4539 presented at Remote Sensing of Clouds and the Atmosphere VI, pp. 62–68, Toulouse, France, 17 Sep.

Bower, K. N., S. J. Moss, D. W. Johnson, T. W. Choularton, J. Latham, P. R. Brown, A. M. Blyth, and J. Cardwell (1996), A parameterization of the ice water content observed in frontal and convective clouds, *Q. J. R. Meteorol. Soc.*, *122*, 1815–1844.

Bühl, J., P. Seifert, A. Myagkov, and A. Ansmann (2016), Measuring ice- and liquid-water properties in mixed-phase cloud layers at the Leipzig Cloudnet station, *Atmos. Chem. Phys.*, *16*, 10,609–10,620, doi:10.5194/acp-16-10609-2016.

Cerdeña, A., A. González, and J. C. Pérez (2006), Remote sensing of water cloud parameters using neural networks, *J. Atmos. Oceanic Technol.*, *24*, 52–63.

Choi, Y. S., C. H. Ho, J. Kim, and R. S. Lindzen (2010a), Observational diagnosis of cloud phase in the winter Antarctic atmosphere for parameterizations in climate models, *Adv. Atmos. Sci.*, *27*(6), 1233–1245.

Choi, Y. S., R. S. Lindzen, C. H. Ho, and J. Kim (2010b), Space observations of cold-cloud phase change, *Proc. Natl. Acad. Sci. U.S.A.*, *107*(25), 1211–1216.

Choi, Y.-S., C.-H. Ho, C.-E. Park, T. Storelvmo, and I. Tan (2014), Influence of cloud phase composition on climate feedbacks, *J. Geophys. Res. Atmos.*, *119*, 3687–3700, doi:10.1002/2013JD020582.

Chubb, T. H., J. B. Jensen, S. T. Siems, and M. J. Manton (2013), In situ observations of supercooled liquid clouds over the Southern Ocean during the HIAPER Pole-to-Pole Observation (HIPPO) campaigns, *Geophys. Res. Lett.*, *40*, 5280–5285, doi:10.1002/grl.50986.

Doutriaux-Boucher, M., and J. Quaas (2004), Evaluation of cloud thermodynamic phase parametrizations in the LMDZ GCM by using POLDER satellite data, *Geophys. Res. Lett.*, *31*, L06126, doi:10.1029/2003GL019095.

Eiben, A. E., and J. E. Smith (2003), *Introduction to Evolutionary Computing, Nat. Comput. Ser.*, 1st ed., Springer, Berlin.

Fan, J., J. M. Comstock, M. Ovchinnikov, S. A. McFarlane, G. McFarquhar, and G. Allen (2010), Tropical anvil characteristics and water vapor of the tropical tropopause layer: Impact of heterogeneous and homogeneous freezing parameterizations, *J. Geophys. Res.*, *115*, D12201, doi:10.1029/2009JD012696.

Findeisen, W. (1938), Die kolloidmeteorologischen Vorgänge bei der Niederschlagsbildung (Colloidal meteorological processes in the formation of precipitation), *Meteorol. Z.*, *55*, 121–133, (Translated and edited by Volken, E., A.M. Giesche, S. Brönnimann. Meteorologische Zeitschrift 24 (2015)).

Fleishauer, R. P., V. E. Larson, and T. H. Vonder Haar (2002), Observed microphysical structure of midlevel, mixed-phase clouds, *J. Atmos. Sci.*, *59*, 1779–1804, doi:10.1175/1520-0469(2002)059<1779:OMSOMM>2.0.CO;2.

Forbes, R. M., and M. Ahlgrimm (2014), On the representation of high-latitude boundary layer mixed-phase cloud in the ECMWF global model, *Mon. Weather Rev.*, *142*(9), 3425–3445.

Giraud, V., O. Thouron, J. Riedi, and P. Goloub (2001), Analysis of direct comparison of cloud top temperature and infrared split window signature against independent retrievals of cloud thermodynamic phase, *Geophys. Res. Lett.*, *28*, 983–986.

Goldberg, E. (1989), *Genetic Algorithms in Search, Optimization and Machine Learning*, Addison-Wesley pp., Reading, Mass.

Hallett, J., and S. C. Mossop (1974), Production of secondary ice particles during the riming process, *Nature*, *249*, 26–28.

Heidinger, A. K., and M. J. Pavolonis (2009), Gazing at cirrus clouds for 25 years through a split window. Part I: Methodology, *J. Appl. Meteorol. Climatolo.*, *48*(6), 1100–1116.

Heidinger, A. K., M. J. Foster, A. Walther, and X. Zhao (2014a), The Pathfinder Atmospheres-Extended AVHRR climate dataset, *Bull. Am. Meteorol. Soc.*, *95*(6), 909–922.

Heidinger, A. K., M. J. Foster, A. Walther, X. Zhao, and NOAA CDR Program (2014b), *NOAA Climate Data Record (CDR) of cloud properties from AVHRR Pathfinder Atmospheres—Extended (PATMOS-x), version 5.3*, NOAA National Centers for Environmental Information, doi:10.7289/V5348HCK.

Hogan, R. J., P. N. Francis, H. Flentje, A. J. Illingworth, M. Quante, and J. Pelon (2003), Characteristics of mixed-phase clouds. I: Lidar, radar and aircraft observations from CLARE'98, *Q. J. R. Meteorol. Soc.*, *129*(592), 2089–2116.

Hoose, C., and O. Möhler (2012), Heterogeneous ice nucleation on atmospheric aerosols: A review of results from laboratory experiments, *Atmos. Chem. Phys.*, *12*, 9817–9854, doi:10.5194/acp-12-9817-2012.

Hu, Y., S. Rodier, K. Xu, W. Sun, J. Huang, B. Lin, P. Zhai, and D. Josset (2010), Occurrence, liquid water content, and fraction of supercooled water clouds from combined CALIOP/IIR/MODIS measurements, *J. Geophys. Res.*, *115*, D00H34, doi:10.1029/2009JD012384.

Jin, H., and S. L. Nasiri (2014), Evaluation of AIRS cloud-thermodynamic-phase determination with CALIPSO, *J. Appl. Meteorol. Climatol.*, *53*, 1012–1027, doi:10.1175/JAMC-D-13-0137.1.

Kahn, B. H., et al. (2014), The Atmospheric Infrared Sounder version 6 cloud products, *Atmos. Chem. Phys.*, *14*, 399–426, doi:10.5194/acp-14-399-2014.

Karlsson, K.-G., and E. Johansson (2013), On the optimal method for evaluating cloud products from passive satellite imagery using CALIPSO-CALIOP data: Example investigating the CM SAF CLARA-A1 dataset, *Atmos. Meas. Tech.*, *6*, 1271–1286, doi:10.5194/amt-6-1271-2013.

Kay, J. E., C. Wall, V. Yettella, B. Medeiros, C. Hannay, P. Caldwell, and C. Bitz (2016), Global climate impacts of fixing the Southern Ocean shortwave radiation Bias in the Community Earth System Model (CESM), *J. Clim.*, *29*, 4617–4636, doi:10.1175/JCLI-D-15-0358.1.

Komurcu, M., T. Storelvmo, I. Tan, U. Lohmann, Y. Yun, J. Penner, Y. Wang, X. Liu, and T. Takemura (2014), Intercomparison of the cloud water phase among global climate models, *J. Geophys. Res. Atmos.*, *119*, 337–3400, doi:10.1002/2013JD021119.

Korolev, A. V., G. A. Isaac, S. G. Cober, J. W. Strapp, and J. Hallett (2003), Microphysical characterization of mixed-phase clouds, *Q. J. R. Meteorol. Soc.*, *129*, 39–65.

Korolev, A. V. (2007), Limitations of the Wegener-Bergeron-Findeisen mechanism in the evolution of mixed-phase clouds, *J. Atmos. Sci.*, *64*, 3372–3375.

Larson, V. E., A. J. Smith, M. J. Falk, K. E. Kotenberg, and J.-C. Golaz (2006), What determines altocumulus dissipation time?, *J. Geophys. Res.*, *111*, D19207, doi:10.1029/2005JD007002.

Lawson, R. P., S. Woods, and H. Morrison (2015), The microphysics of ice and precipitation development in tropical cumulus clouds, *J. Atmos. Sci.*, *72*, 2429–2445, doi:10.1175/JAS-D-14-0274.1.

Li, Z., and H. Le Treut (1992), Cloud-radiation feedbacks in a general circulation model and their dependence on cloud modelling assumptions, *Clim. Dyn.*, *7*, 133–139, doi:10.1007/BF00211155.

Lloyd, G., et al. (2015), The origins of ice crystals measured in mixed-phase clouds at the high-alpine site Jungfraujoch, *Atmos. Chem. Phys.*, *15*, 12,953–12,969.

Madonna, E., H. Wernli, H. Joos, and O. Martius (2014), Warm conveyor belts in the ERA-interim dataset (1979–2010). Part I: Climatology and potential vorticity evolution, *J. Clim.*, *27*(1), 3–26.

McCoy, D. T., D. L. Hartmann, M. D. Zelinka, P. Ceppi, and D. P. Grosvenor (2015), Mixed-phase cloud physics and Southern Ocean cloud feedback in climate models, *J. Geophys. Res. Atmos.*, *120*, 9539–9554, doi:10.1002/2015JD023603.

Mitchell, J. F. B., C. A. Senior, and W. J. Ingram (1989), CO_2 and climate: A missing feedback?, *Nature*, *341*, 132–134, doi:10.1038/341132a0.

Morrison, A. E., S. T. Siems, and M. J. Manton (2011), A three-year climatology of cloud-top phase over the Southern Ocean and North Pacific, *J. Clim.*, *24*, 2405–2418, doi:10.1175/2010JCLI3842.1.

Morrison, H., G. de Boer, G. Feingold, J. Harrington, M. D. Shupe, and K. Sulia (2012), Resilience of persistent Arctic mixed-phase clouds, *Nat. Geosci.*, *5*, 11–17, doi:10.1038/ngeo1332.

Naud, C., A. D. Del Genio, and M. Bauer (2006), Observational constraints on cloud thermodynamic phase in midlatitude storms, *J. Clim.*, *19*, 5273–5288.

Naud, C. M., A. Del Genio, M. Haeffelin, Y. Morille, V. Noel, J. C. Dupont, D. D. Turner, C. Lo, and J. Comstock (2010), Thermodynamic phase profiles of optically thin midlatitude clouds and their relation to temperature, *J. Geophys. Res.*, *115*, D11202, doi:10.1029/2009JD012889.

Naud, C. M., and B. H. Kahn (2015), Thermodynamic phase and ice cloud properties in Northern Hemisphere winter extratropical cyclones observed by Aqua AIRS, *J. Appl. Meteorol. Climatol.*, *54*, 2283–2303.

Pallavi, V. P., and V. Vaithiyanathan (2013), Combined artificial neural network and genetic algorithm for cloud classification, *Int. J. Eng. Technol.*, *5*(2), 787–794.

Paukert, M., and C. Hoose (2014), Modeling immersion freezing with aerosol-dependent prognostic ice nuclei in Arctic mixed-phase clouds, *J. Geophys. Res. Atmos.*, *119*, 9073–9092, doi:10.1002/2014JD021917.

Pavolonis, M. J., A. K. Heidinger, and T. Uttal (2005), Daytime global cloud typing from AVHRR and VIIRS: Algorithm description, validation and comparisons, *J. Appl. Meteorol.*, *44*, 804–826.

Phillips, V. T. J., et al. (2005), Anvil glaciation in a deep cumulus updraught over Florida simulated with the explicit microphysics model. I: Impact of various nucleation processes, *Q. J. R. Meteorol. Soc.*, *131*, 2019–2046, doi:10.1256/qj.04.85.

Platnick, S., M. D. King, S. A. Ackerman, W. P. Menzel, B. A. Baum, Riédi J. C., and R. A. Frey (2003), The MODIS cloud products: Algorithms and examples from Terra, *IEEE Trans. Geosci. Remote Sens.*, *41*, 459–473.

Pruppacher, H. R., and J. D. Klett (1997), *Microphysics of Clouds and Precipitation*, 2nd ed., Kluwer Acad., Dordrecht, Netherlands.

Rosenfeld, D., and L. Woodley (2000), Deep convective clouds with sustained supercooled liquid water down to −37.5°C, *Nature*, *405*, 440–442.

Rosenfeld, D., X. Yu, G. Liu, X. Xu, Y. Zhu, Z. Yue, J. Dai, Z. Dong, Y. Dong, and Y. Peng (2011), Glaciation temperatures of convective clouds ingesting desert dust, air pollution and smoke from forest fires, *Geophys. Res. Lett.*, *38*, L21804, doi:10.1029/2011GL049423.

Saha, S., et al. (2010), The NCEP climate forecast system reanalysis, *Bull. Am. Meteorol. Soc.*, *91*, 1015–1057.

Sand, W. R., W. A. Cooper, M. K. Politovich, and D. L. Veal (1984), Icing conditions encountered by a research aircraft, *J. Climatol. Appl. Meteorol.*, *23*, 1427–1440.

Stengel, M., A. Kniffka, J. F. Meirink, M. Lockhoff, J. Tan, and R. Hollmann (2014), CLAAS: The CM SAF cloud property data set using SEVIRI, *Atmos. Chem. Phys.*, *14*, 4297–4311, doi:10.5194/acp-14-4297-2014.

Stengel, M., et al. (2015), The Cloud Climate Change Initiative: Assessment of state-of-the-art cloud property retrieval schemes applied to AVHRR heritage measurements, *Remote Sens. Environ.*, *162*, 363–379, doi:10.1016/j.rse.2013.10.035.

Stubenrauch, C. J., et al. (2013), Assessment of global cloud datasets from satellites: Project and database initiated by GEWEX radiation panel, *Bull. Am. Meteorol. Soc.*, *94*, 1031–1049.

Tan, I., and T. Storelvmo (2016a), Sensitivity study on the influence of cloud microphysical parameters on mixed-phase cloud thermodynamic phase partitioning in CAM4, *J. Atmos. Sci.*, *73*, 709–728.

Tan, I., T. Storelvmo, and M. D. Zelinka (2016b), Observational constraints on mixed-phase clouds imply higher climate sensitivity, *Science*, *352*(6282), 224–227.

Waliser, D. E., et al. (2009), Cloud ice: A climate model challenge with signs and expectations of progress, *J. Geophys. Res.*, *114*, D00A21, doi:10.1029/2008JD010015.

Williams, E., et al. (2002), Contrasting convective regimes over the Amazon: Implications for cloud electrification, *J. Geophys. Res.*, *107*(D20), 8082, doi:10.1029/2001JD000380.

Wilson, T. W. et al. (2015), A marine biogenic source of atmospheric ice-nucleating particles, *Nature*, *525*, 234–238, doi:10.1038/nature14986.

Winker, D. M., et al. (2010), The CALIPSO mission: A global 3D view of aerosols and clouds, *Bull. Am. Meteorol. Soc.*, *91*(9), 1211–1229.

Wolters, E. L., R. A. Roebeling, and A. J. Feijt (2008), Evaluation of cloud-phase retrieval methods for SEVIRI on Meteosat-8 using ground-based lidar and cloud radar data, *J. Appl. Meteorol. Climatol.*, *47*(6), 1723–1738.

Xiong, X., D. Lubin, W. Li, and K. Stamnes (2002), A critical examination of satellite cloud retrieval from AVHRR in the Arctic using SHEBA data, *J. Appl. Meteorol.*, *41*(12), 1195–1209, doi:10.1175/1520-0450(2002)041<1195:ACEOSC>2.0.CO;2.

Yuan, T., J. Vanderlei-Martins, Z. Li, and L. A. Remer (2010), Estimating glaciation temperature of deep convective clouds with remote sensing data, *Geophys. Res. Lett.*, *38*, L09704, doi:10.1029/2010GL042753.

Yao, X., Y. Liu, and G. Lin (1999), Evolutionary programming made faster, *IEEE Trans. Evol. Comput.*, *3*(2), 82–102.